# EFFECT OF INLET CONDITIONS ON THE THERMAL INSULATION PERFORMANCE OF MARINE GAS TURBINE EXHAUST SYSTEMS

by

***Zongwei ZHANG[a], Hao CHEN[a], Cong LIU[b], and Qingkun MENG[c*]***

[a]College of Aeronautical Engineering, Civil Aviation University of China, Tianjin, China
[b]College of Air Traffic Management, Civil Aviation University of China, Tianjin, China
[c]System Design Institute of Mechanical-Electrical Engineering, Beijing, China

Original scientific paper
https://doi.org/10.2298/TSCI240206160Z

*A marine gas turbine insulation solution was designed to reduce exhaust system temperatures. The effects of cooling gas temperature (45 °C, 55 °C, 65 °C), cooling air velocity (2-10 m/s), and a range of classic aerodynamic conditions ranging on the thermal insulation performance of the gas turbine exhaust system were investigated using numerical simulations. The results indicate that the use of aerogel insulation material effectively reduces the average temperature of the exterior volute casing to 71 °C from 315 °C under rated turbine conditions. The exterior volute casing temperature increases with higher cooling gas inlet temperatures but decreases with increasing cooling gas inlet velocities. Additionally, alterations in the aerodynamic conditions at the gas inlet will induce changes in the thermal insulation performance of the exhaust system, and excessive circumferential flow velocities can cause localized overheating in the exhaust volute casing.*

Key words*: marine gas turbine engine, exhaust volute, thermal protection, aerogel, numerical simulation*

## Introduction

Gas turbine engines, as power devices for maritime propulsion, have been in use since the previous century [1]. Compared to internal combustion engines and steam turbines, gas turbines exhibit several advantages, including higher single-unit power, lower weight, smaller size, rapid startup, acceleration, and the ability to achieve cascade utilization of energy. Due to the absence of reciprocating moving parts, gas turbines experience reduced mechanical vibration-induced damage, resulting in improved operational reliability [2-4]. The exhaust volute casing of marine gas turbine engines serves as a critical component connecting the power turbine to the exhaust system. It functions to collect and decelerate the exhaust gases expelled from the power turbine, redirecting the air-flow [5]. The outlet of the exhaust volute casing is connected to the exhaust duct of the gas turbine power unit, ultimately venting the exhaust gases from the power turbine into the atmosphere. Whether it is the main marine gas turbine engine that generates propulsion power or auxiliary gas turbine engines driving shipboard machinery, all of them challenges related to high exhaust temperatures, increased resistance, limited design

*Corresponding author, e-mail: mengqingkun061636@163.com

space, and tonnage constraints. The high temperature and high velocity exhaust flow impinging on the exhaust volute casing leads to elevated casing temperatures. These excessively high temperatures can result in elevated temperatures within the ship's compartments, which are unfavorable for personnel operations and may even pose risks to personnel safety [6]. Additionally, compared to land-based gas turbines, shipboard gas turbines often require smaller-scale insulation solutions to meet the constraints of onboard spaces. The existing research on insulation for marine gas turbine exhaust systems is scant. Therefore, this paper aims to explore an exhaust insulation scheme that can withstand extreme temperatures at the turbine outlet, occupies minimal space, and exhibits excellent insulation performance. This research holds significant implications for the development of marine gas turbines.

In the industrial domain, there exists a substantial body of research outcomes pertaining to thermal insulation schemes and insulating performance of gas turbines. Park *et al*. [7] investigated heat transfer and temperature distribution within micro gas turbine systems. Moreover, various insulation materials were utilized to regulate temperature levels on the baseplate. To evaluate the impact of thermal conductivity on the generator and micro gas turbine, the insulation material's thermal conductivity was varied between 0.1 W/mK and 100 W/mK. Singh *et al*. [8] proposes an air diffuser for gas turbine exhaust systems and explores three design strategies for reducing exhaust gas temperatures using slots in numerical simulations. Optimizing the slot parameters can enhance the diffuser's cooling efficiency. Park *et al*. [9] introduced a thermal insulation scheme for a micro gas turbine generator. Given the high turbine temperatures of up to 700 °C, Zirconia ($ZrO_2$) was selected as the insulation material to keep the generator's temperature below 50 °C without affecting the performance of NdFeB permanent magnets. Vinay and Chakravarthy [10] examined insulation techniques for exhaust ducts in aircraft engines to mitigate the heating of short compartments adjacent to exhaust pipes. Experimental validation was conducted by covering the insulation material. The findings revealed that the surface aluminum materials in the short compartments satisfied the target temperature requirements. Xu *et al*. [11] studied the heat transfer mechanisms within the auxiliary power unit (APU) compartment of aircraft and analyzed its structure. The study revealed that the temperature rise within the compartment was primarily due to radiative heat transfer, and APU fire shields and exhaust insulation covers contributed to radiative insulation.

With the advancement of material technology, a variety of high-performance materials are being integrated into thermal insulation solutions in industrial design. Nano-porous materials such as aerogels, as multifunctional materials, have found extensive applications in fields such as physics, chemistry, aerospace, and new energy [12]. Aerogel-based porous composite insulation materials exhibit properties such as high surface area, low density, and high porosity [13]. Importantly, their thermal conductivity, even at standard temperature and pressure, can be lower than that of free air. Consequently, nano-porous insulation materials are often referred to as super-insulating materials [14], offering significant potential for applications in thermal insulation, energy conservation, and safety protection in low temperature engineering and extreme high temperature environments. Dai *et al*. [15] studied the influence of cracking gas on the heat transfer of $SiO_2$ aerogel using experimental and numerical methods. With the increase of working pressure, the influence of cracking gas permeation on the heat transfer of $SiO_2$ aerogel is mitigated due to the increase of gas density stored in $SiO_2$ aerogel. The thermal insulation performance of $SiO_2$ aerogel-based insulation systems will be better under higher working pressure conditions. Heye *et al*. [16] proposed a versatile component based on fiber-reinforced silica aerogel for exhaust system insulation, aiming to maintaining exhaust gases at high

temperatures to enhance the effectiveness of catalytic systems. Fesmire and Sass [17] demonstrated a space launch rocket solution employing aerogel beads to address thermal insulation challenges for liquid hydrogen ($LH_2$) internal tank models of space shuttle external tanks. Li *et al*. [18] introduced an innovative design of integrated structures and insulation materials based on silica aerogels for thermal insulation under the extreme conditions of the Martian surface environment.

This paper proposes a thermal insulation solution for marine gas turbine exhaust systems. Aerogel-based materials are employed as the insulation material. Numerical simulations are employed to optimize the flow field of the insulation scheme. The insulation's effectiveness is evaluated by analyzing the exterior volute casing temperature under varying cooling gas inlet temperatures (45 ℃, 55 ℃, 65 ℃), cooling gas inlet velocities (2-10 m/s), and five representative aerodynamic conditions. To predict heat transfer and temperature distribution, the commercial code FLUENT-18 was employed for convective and thermal calculations. A combined experimental and simulation approach was utilized to determine the adoption of the Realizable $k$-$\varepsilon$ model coupled with standard wall functions as the turbulence model. The results indicate that the insulation scheme effectively controls the exterior volute casing temperature, providing reliable temperature management.

## Model and design

Figure 1 depicts a schematic of the gas turbine exhaust system, which consists of an enclosure and an exhaust volute casing. The exhaust volute casing measures 3.8 m in both height and width. The exhaust volute casing connects to the gas turbine outlet at one end and

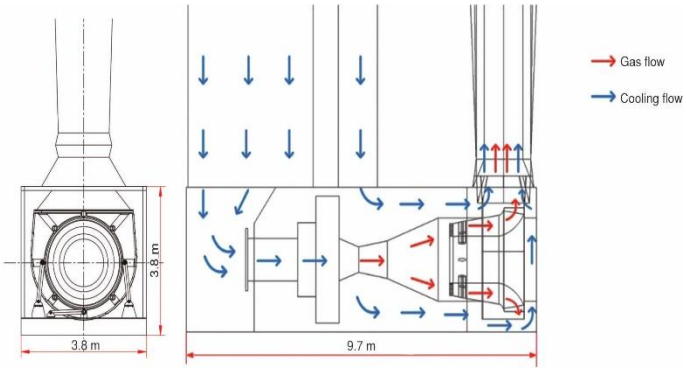


**Figure 1. Gas turbine exhaust system schematic and flow direction diagram structure composition**

to the power unit exhaust duct at the other end. The exhaust gases from the gas turbine ultimately pass through the exhaust volute casing and enter the atmosphere through the exhaust duct. To prevent the exhaust system from reaching excessive temperature a box-type volute casing has been widely employed. This design entails encapsulating the exhaust volute casing with an enclosure and injecting low temperature ambient air within the enclosure. At the outlet of the exhaust volute casing, high temperature exhaust gases are mixed with low temperature cooling air before entering the exhaust duct. The external air-flow passes through the enclosure, introducing cool air to the exhaust volute casing's exterior. Following the cooling of the exterior casing, the air-flow bends at a 90° angle and ascends through the converging section before entering the exhaust duct.

Figure 2 illustrates the various structure composition of the exhaust volute casing. The exhaust volute casing is divided into several sections: the expansion section, straight turning section, front support wall, rear support wall, sidewalls, and the converging section. High temperature internal gas flow egresses from the turbine and enters the exhaust volute casing through the straight turning section, executes a 90° bend, and subsequently ascends through the converging section before entering the exhaust duct. To further reduce the exterior casing surface temperature, it is necessary to cover the exterior casing with nano-aerogel-based insulation material.

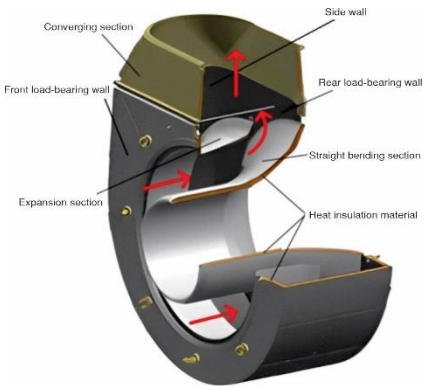


**Figure 2. Exhaust volute internal flow and**

As shown in fig. 3, the insulation material used in this study is a composite of aerogel particles and silica fibers. The density is 187 kg/m³. The temperature-dependent real thermal conductivity of the insulation material was experimentally determined in the Thermal Management Laboratory of Civil Aviation University of China. The laboratory used a high-temperature thermal conductivity meter, model DRS-3A, as shown in fig. 4. The experiment used a steady-state method to measure the effective thermal conductivity of the insulation material, culminating in the determination of the functional relationship between the thermal conductivity of this type of insulation material and temperature, expressed as:

**Figure 3. Insulation material unit**

$$\lambda_{\text{ture}}(t) = 0.9880 - 0.0053t + 9.5164\times10^{-6}t^2 - 4.8831\times10^{-9}t^3$$

## Mesh and boundary conditions

To evaluate the thermal insulation performance of the exhaust system, the following settings were implemented, adhering to a consistent mesh configuration and boundary conditions. The exhaust system region was partitioned into three distinct domains. The internal flow domain, the solid domain, and the external flow domain. The solid domain comprises the metallic exhaust volute casing and the insulation material adhered to the metallic walls. The inlet of the exhaust volute casing serves as the internal flow inlet, utilizing a mass-flow inlet boundary condition. The inlet of the enclosure serves as the external flow inlet, employing a velocity inlet boundary condition. The system's outlet is configured as a mixed outlet after combining the internal and external flows, and is specified as a pressure outlet. The materials of the exhaust system casing and the exhaust volute casing are $OCr_{18}Ni_9Ti$ stainless steel. The exhaust volute casing measures 6 mm in thickness, while

**Figure 4. The DRS-3A high temperature thermal conductivity meter**

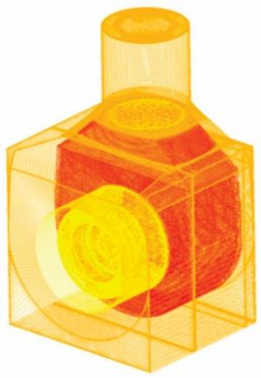

**Figure 5. Overall mesh of the exhaust system**

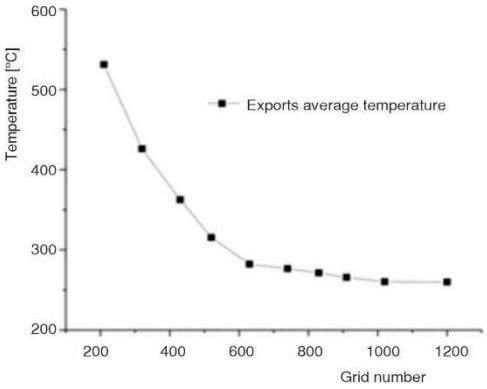


**Figure 6. Outlet average temperature *vs.* number of mesh cells**

the insulation material measures 50 mm in thickness, ensuring effective thermal insulation. The mesh is shown in fig. 5.

An integrated model was established using the interface method, and numerical computations were conducted. Structured grids were used for block-wise grid division. For both the internal and external flow domains, air was employed as the working fluid. However, due to the potential for flow velocities exceeding 200 m/s in both the internal and external domains, compressibility effects arising from the high-speed flow had to be considered. Therefore, the working fluid was modeled as an ideal gas with variable density to account for compressibility effects. The grids for the internal flow, external flow, and solid domain were combined to form the 3-D mesh of the final fluid-structure integrated model. Under the specified operational parameters, the exhaust gas temperature at the exit of the exhaust system was used as the measurement object, and the results are presented in fig. 6. After reaching 8.3 million grid cells, the variation in the average outlet temperature becomes relatively low. Therefore, a grid size of 8.3 million was chosen for the model. The external flow calculation domain consisted of approximately 4.342 million grid cells, while the internal flow calculation domain comprised approximately 2.955 million grid cells. Within the solid domain, the metallic wall contained approximately 840000 grid cells, while the insulation material incorporated approximately 1.169 million grid cells. The total number of grid cells in the model was approximately 8.3 million.

Table 1 presents the state parameters of high temperature gases at the turbine outlet of the gas turbine, corresponding to the inlet cross-section of the exhaust volute. In these five operating conditions, the mass-flow rate gradually increases, the total temperature remains essentially constant, and the total pressure gradually increases. The axial component of the velocity vector exhibits a gradual increase, while the circumferential component gradually decreases, and the radial component gradually decreases. The flow state of the gas flow at the inlet of the volute gradually changes from turbulent to laminar, as shown in fig. 7. The standard working condition of gas inlet is Case 5, and the standard temperature and pressure in a ship are 55 ℃ and 99.725 kPa, respectively.

**Table 1. In-inlet parameters under different working conditions**

| Working condition | $q_m$, [kgs$^{-1}$] | $P_{total}$ [KPa] | $P_{static}$ [Kpa] | $T_{total}$ [°C] | $V_{axial}$ [ms$^{-1}$] | $V_{circ}$ [ms$^{-1}$] | $V_{radial}$ [ms$^{-1}$] |
|---|---|---|---|---|---|---|---|
| Case 1 | 33.4 | 102.436 | 93.8 | 347.85 | 54.3 | –160.253 | 15.2 |
| Case 2 | 43.58 | 102.9 | 94.54 | 352.05 | 62.1 | –159.7 | 7.2 |
| Case 3 | 70.97 | 106.44 | 101.74 | 379.55 | 99.6 | –79.8 | 4.6 |
| Case 4 | 81.57 | 108.31 | 103.87 | 399.55 | 1161 | –45.2 | 2.6 |
| Case 5 | 90.99 | 110.21 | 105.25 | 421.95 | 132.3 | –11.5 | 0.6 |

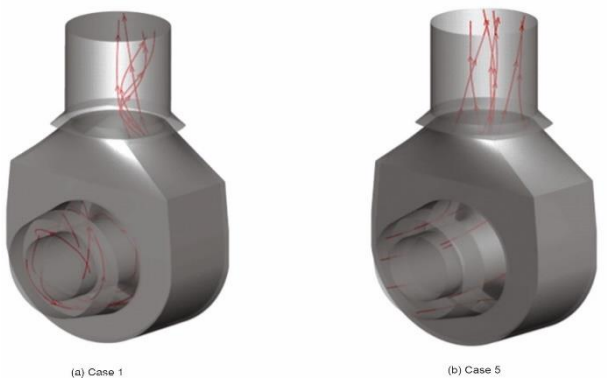


**Figure 7. Velocity vector map of the gas inlet of the volute; (a) Case 1 and (b) Case 5**

## Turbulence models

To ensure the reliability of numerical simulation results, it is necessary to study the use of turbulence models and wall functions. This paper employs the method of comparing experimental data with numerical simulations. The experimental system design is illustrated in fig. 8, while the experimental setup is depicted in fig. 9. The steady-state experiments were

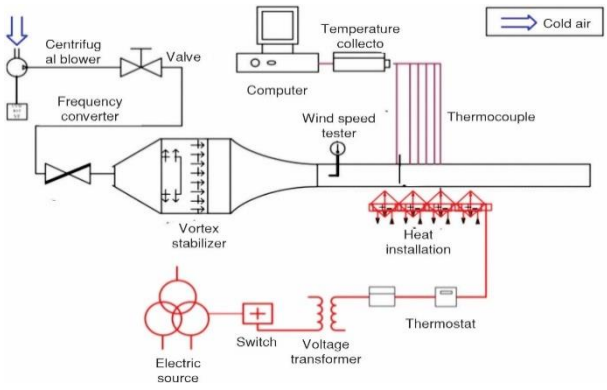


**Figure 8. Verification experiment system diagram**

conducted using the same insulation material, as shown in fig. 10. An electric heater was installed inside the cylindrical insulation model (50 mm insulation material and 6 mm $OCr_{18}Ni_9Ti$) to maintain the wall temperature of the insulation material at 600 °C. The insulation material was positioned within an airflow field maintained at a constant temperature of 40 °C and velocities of 2 m/s, 3 m/s, 4 m/s, and 5 m/s. The wall temperature was measured and recorded by thermocouples attached to the outer surface of the insulation material. Then, six combinations of turbulence models and wall functions were used to

**Figure 9. Experimental set-up diagram for validation**

**Figure 10. Thermal insulation material testing unit with metal heater**

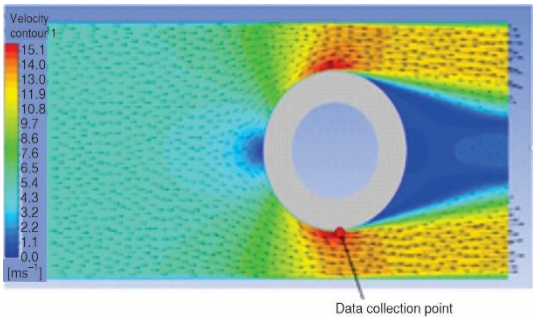


**Figure 11. Numerical flow field diagram of cylindrical insulation material**

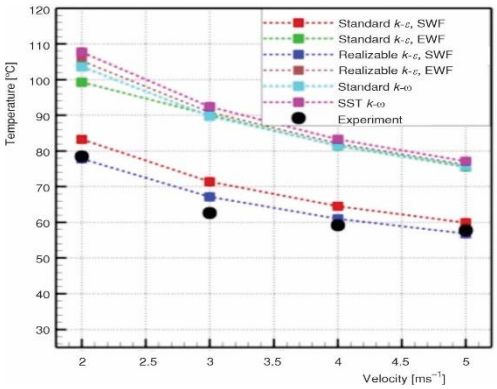


**Figure 12. Variation of temperature calculated by six turbulence models and experimental observation with velocity**

conduct numerical simulations with the same experimental model, and the temperatures at the observation points were compared with the experiments. The data acquisition locations and numerical simulation flow field diagram are shown in fig. 11.

As shown in fig. 12, six turbulence models were utilized: *k-ε* standard model with standard wall functions, *k-ε* standard model with enhanced wall functions, realizable *k-ε* model with standard wall functions, realizable *k-ε* model with enhanced wall functions, *k-ω* standard model, and *k-ω* SST model. The results indicate that the realizable *k-ε* model with standard wall functions demonstrates good agreement between the calculated thermal coupling results for two different types of insulation materials and the experimental data. The selection of the realizable *k-ε* model, based on the *k-ε* two-equation model, is suitable for fully developed turbulent flows and is specifically designed for high Reynolds number turbulent flows. It requires special treatment for low Reynolds number flows and near-wall flow regions, necessitating the use of wall functions, such as the standard wall function, for near-wall flow and heat transfer solutions. The simple pressure-velocity coupling algorithm was employed, and spatial discretization of the convective term used the least squares cell-based method. second-order schemes were applied for the pressure and momentum equations, while first-order upwind schemes were employed for turbulence kinetic energy, turbulent dissipation rate, and energy equations.

## Results and discussion

To verify the feasibility of the insulation solution, the volute gas inlet was operated under the standard operating condition, Case 5. The cooling air-flow velocity was set to 5 m/s and the cooling air-flow temperature was set at 55 ℃.

Figure 13 displays the variation in the outer surface temperature of the exhaust volute casing before and after the addition of insulation material. Figure 14 provides a detailed account of the average temperature changes in different sections of the exhaust volute casing. The results reveal that the addition of insulation material significantly enhances the thermal insulation. Following the implementation of insulation measures, the temperatures of various sections of

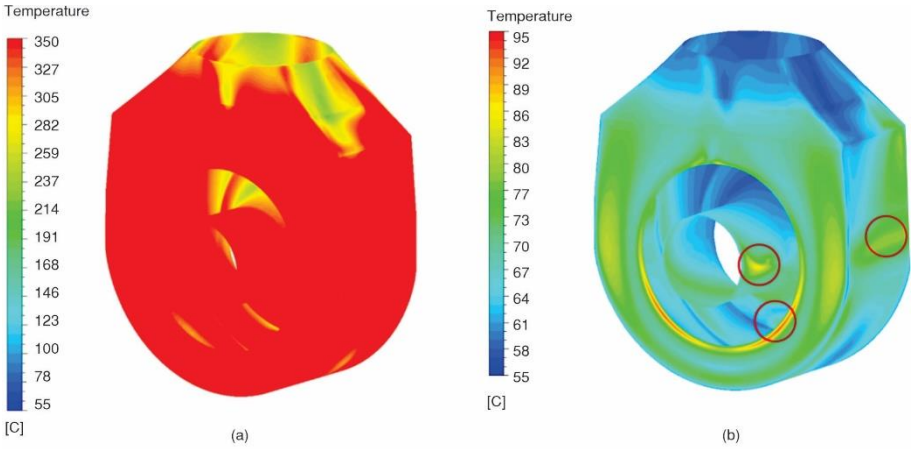


**Figure 13. (a) Temperature contour plot of uninsulated exhaust cowling outer wall and (b) temperature contour plot of insulated exhaust cowling outer wall**

the exhaust volute casing decreased noticeably, resulting in an average temperature reduction of 244 ℃. After insulation measures were applied, the average temperature of the exhaust volute casing reduced to 71 ℃, with the highest temperature observed on the front wall (92.2 ℃). Compared to the situation before insulation, the thermal insulation has a significant impact. The temperatures of the exhaust volute casing have all dropped to below 100 ℃. Further cooling through the external flow casing of the exhaust system ensures the safety of personnel working inside the compartment.

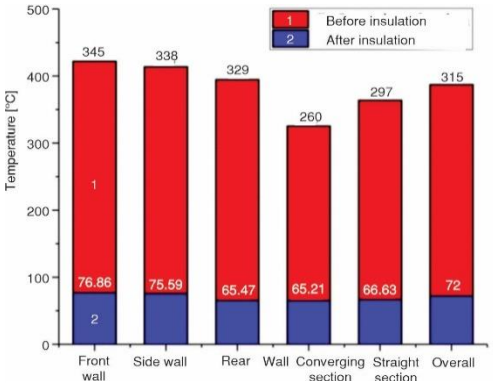


**Figure 14. Comparison of temperatures in various sections of the exhaust cowling before and after insulation**

The insulation treatment results in the formation of localized hot spots, as shown in fig. 13. The hot spots are located at the front wall gas inlet (94.3 ℃), the side wall section (92.1 ℃), and the straight bend section (87.2 ℃). The temperature of the hot spots is approximately 20 ℃ higher than the overall average temperature. The high temperature at the front wall is due to the proximity to the heat source and the conduction of heat through the volute. The elevated temperature at the side wall section is due to the reduced air-flow velocity caused by the small gap between the volute and the casing, as shown in fig. 15(a). The high temperature at the straight bend section is due to the excessive gap between the volute and the casing, which results in low air-flow velocity and poor heat transfer, as shown in fig. 15(b).

To verify the impact of the inlet parameters on the thermal insulation performance of the exhaust system, adjustments were made to the boundary conditions. First, the effect of cooling air-flow inlet temperature on insulation performance was investigated. The gas inlet operating condition was maintained at Case 5, the cooling air-flow velocity was set at 5 m/s, and the air-flow temperature was changed to 45 ℃, 55 ℃, and 65 ℃, respectively. Figures 16(a) and 16(b) show the variations in the average and maximum temperatures of the insulation material outer surface in varying cooling air-flow inlet temperature conditions.

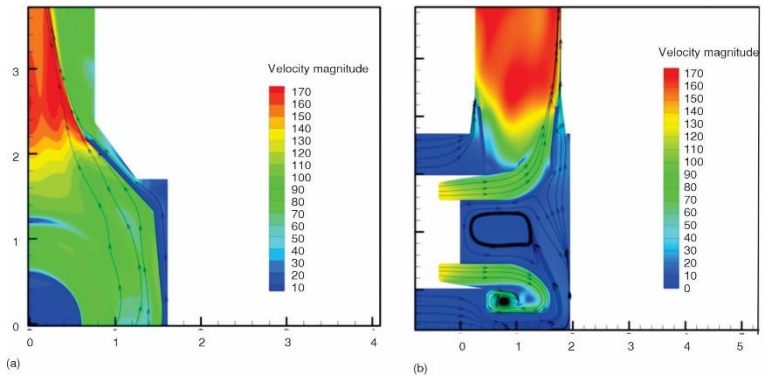


**Figure 15. Cross-sectional velocity cloud diagram and streamlines in the volute; (a) *X*-cross-sectional and (b) *Y*-cross-sectional**

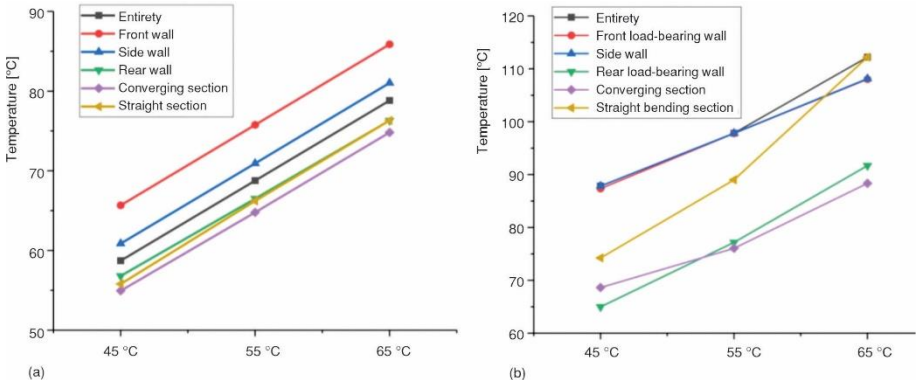


**Figure 16. (a) Variation of the average temperature of the outer wall surface of the volute with cooling air temperature and (b) variation of the maximum temperature of the outer wall surface of the volute with cooling air temperature**

The fig. 17 illustrate that the cooling gas temperature has a significant impact on the outer surface temperature of the insulation material. As the cooling gas temperature increases, the outer surface temperature of the insulation material gradually rises, resulting in a temperature, for every 10 ℃ increases in the inlet air temperature, both the overall temperature and individual component temperatures increase by 10 ℃, exhibiting a strong positive linear correlation. When the cooling temperature is set at 65 ℃, the overall average temperature reaches 78.82 ℃. The region with the highest local average temperature is the front wall, with an average temperature of 85.87 ℃. However, when considering the highest temperature, there is no linear correlation between the inlet air velocity and the outer wall temperature. Under the 65 ℃ conditions, the highest local temperatures in these three areas are 108.03 ℃, 108.14 ℃, and 112.20 ℃, respectively.

To investigate the effect of cooling air-flow velocity on insulation performance, the gas inlet aerodynamic condition was maintained at Case 5 and the cooling air-flow temperature was set to the standard cabin temperature of 55 ℃. The cooling air-flow velocity was changed to 2 m/s to 10 m/s. The relationship between the volute outer surface temperature and cooling gas velocity is shown in fig. 14.

The cooling air-flow velocity has a significant impact on the insulation effect. As the cooling air velocity increases, the outer surface temperature of the insulation material of the

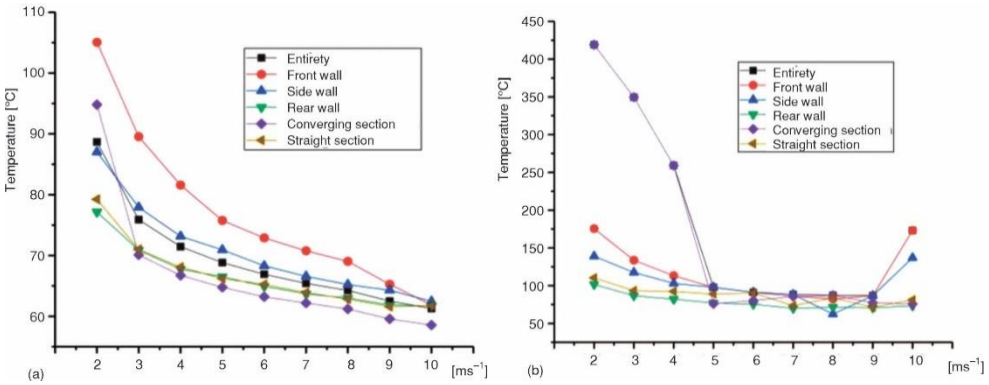


**Figure 17. (a) Variation of the average temperature of the outer wall surface of the volute with cooling air velocity and (b) variation of the maximum temperature of the outer wall surface of the volute with cooling air velocity**

exhaust volute gradually decreases. With respect to the average temperature, the most substantial overall average temperature reduction occurred when the inlet cooling air-flow velocity increased from 2 m/s to 5 m/s. The average temperature decreased from 89.4 ℃ to 71 ℃. The maximum temperature of the volute decreased to below 100 ℃ when the cooling air-flow velocity reached 5 m/s. However, local hot spots were observed in the converging section when the cooling air-flow velocity was below 5 m/s. Figure 18 shows the temperature diagram and air-flow streamlines in the volute under different cooling air-flow velocities. As shown in the figure, the local hot spots are caused by the reverse flow of hot gas into the outer wall of the volute due to the low cooling air-flow velocity and high gas flow velocity. The reverse flow phenomenon does not occur when the cooling air-flow velocity reaches 5 m/s.

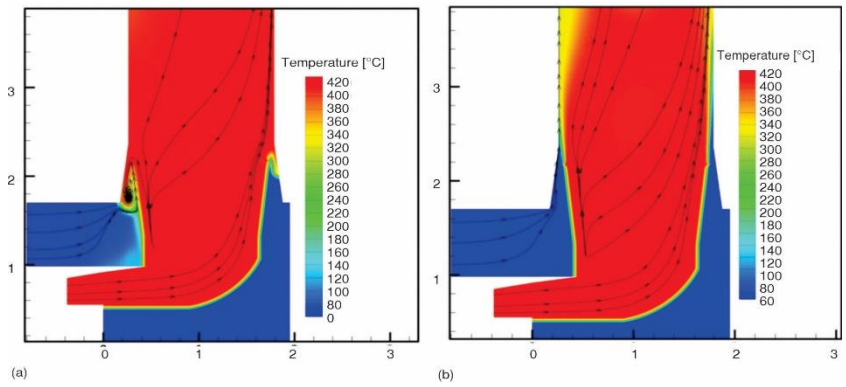


**Figure 18. Cross-sectional temperature cloud diagram and streamlines of the exhaust volute; (a) 2 m/s and (b) 7 m/s**

Figure 19(a) depicts the trend in air-flow velocity on the outer surface of the exhaust volute, while fig. 19(b) illustrates the variation in convective heat transfer coefficients on the outer surface of the exhaust volute. The formula for calculating the convective heat transfer coefficient is derived from the following equation:

$$HTC = \frac{q}{T_{\text{wall}} - T_{\text{out}}} \tag{1}$$

where $T_{wall}$ is the temperature of the insulation material's outer surface and $T_{out}$ – the outlet temperature, which is fixed at 55 °C. Heat flux and wall temperature can be calculated through simulation.

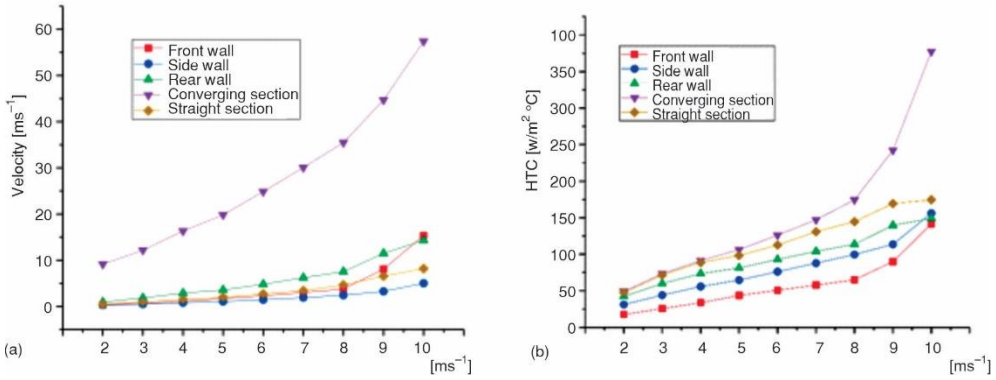


**Figure 19. (a) Surface velocity of the outer wall of the volute and (b) convective heat transfer coefficient of the outer surface of the volute**

From figs. 19(a) and 19(b), as the inlet velocity of the cooling air increases, the average air-flow velocity on the outer surface of the insulation material of the volute gradually increases. Correspondingly, the convective heat transfer coefficient also gradually increases, but there is a significant unevenness between different regions. The surface air-flow velocity of the converging section is highest, and the surface air-flow velocity of the sidewall section is lowest. Similarly, the convective heat transfer coefficient is highest in the converging section, while those of the front wall and sidewall are relatively low. This is attributed to the narrowness of the local region, which restricts air-flow circulation.

To examine the impact of the gas inlet's aerodynamic conditions on the exhaust system's insulation performance, the cooling air's velocity and temperature are maintained at a constant 55 °C, the standard cabin temperature, and a speed of 5 m/s. Subsequently, the five working conditions are individually incorporated into the numerical simulation calculations. From fig. 20, it is evident that the outer surface temperature of the insulation material increases with the increase in the internal flow inlet condition coefficient. Both the overall and individual average temperatures exhibit a positive correlation with the condition coefficient. Case 5 represents the standard rated thrust condition, while Cases 1-4 represent other operating conditions below the standard. From the perspective of average temperature, an increase in inlet mass-flow rate and total temperature leads to a decrease in thermal insulation effectiveness.

The front wall and side walls show an increasing trend with the condition coefficient, and the high temperature regions are primarily concentrated in the center of the front bearing wall and the lower part of the side walls. In contrast, the temperature in the rear wall, converging section, and straight bending section fluctuates considerably. Through analysis, it is concluded that these phenomena may have multiple causes. This caused includes changes in the direction of the air inlet velocity vector with the increasing condition coefficient, as well as the presence of small vortex flows within certain regions of the exhaust volute due to the variation in internal flow as the condition coefficient increases.

Figure 21 displays the velocity vectors and temperature distributions at different internal flow conditions across the exhaust volute. As evident from fig. 21, in the range from condition Case 1 to Case 3, the substantial initial radial air-flow causes the internal flow gas to

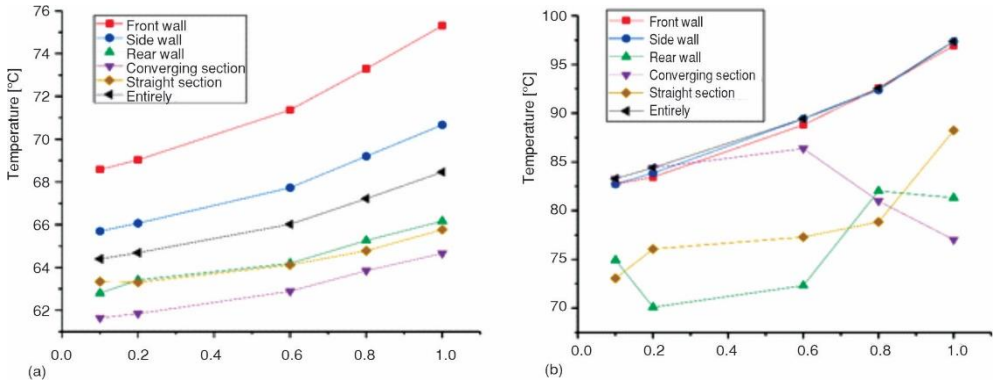


**Figure 20. (a) Surface velocity of the outer wall of the volute and (b) convective heat transfer coefficient of the outer surface of the volute**

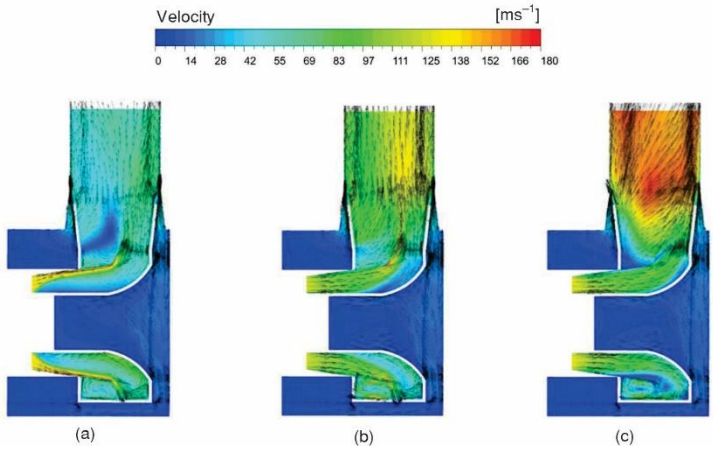


**Figure 21. (a) Case 1, (b) Case 2, and (c) Case 3; vector distribution at the midsection under different operating conditions**

preferentially rotate along the expanding section walls of the casing. Consequently, distinct high velocity and low velocity regions become apparent. Air-flow that flows out near the expanding section's walls mostly enters the converging section when passing through the turning section. This leads to lower air-flow velocity in the areas of the front bearing wall, straight bending section, and rear bearing wall, creating a low velocity region. Consequently, the center part of the front bearing wall, most of the straight bending section, and the rear bearing wall exhibit higher temperatures. In the range from Case 3 to Case 5, the radial air-flow velocity decreases, and the air-flow is primarily in the axial direction. At this point, the air-flow velocity is relatively high, and the high temperature air-flow directly impacts the straight bending section. However, in this region, the external cooling air-flow has a very low air-flow velocity, leading to elevated temperatures. As the air-flow passes from the expanding section into the turning section, only a limited amount of air-flow goes through the front bearing wall, resulting in a distinct low velocity region and higher temperatures in the center of the front bearing wall. The high temperature region on the side walls is primarily concentrated at the bottom centerline. As the air-flow enters the turning section from below the expanding section, the internal flow gas directly impinges on the casing's lower wall, and the narrow gap between the casing and

the box body in this area results in ineffective heat transfer, ultimately leading to elevated temperatures.

## Conclusions

The study introduces a thermal insulation method based on nano-aerogel material, which effectively safeguards the exhaust system of marine gas turbines. Under rated operating conditions, this method reduces the outer surface temperature of the exhaust volute casing from 315 °C to 71 °C. It achieves efficient thermal insulation within the constraints of limited ship compartment space.

The effectiveness of the exhaust system's thermal insulation is influenced by three main factors: cooling gas temperature, cooling gas inlet air-flow velocity, and internal exhaust flow conditions. Higher cooling gas temperatures and elevated internal exhaust flow conditions diminish insulation effectiveness, while higher cooling gas inlet air-flow velocities enhance insulation performance.

During low-power operation of the gas turbine, the circumferential velocity of the exhaust flow within the exhaust volute casing is relatively high, giving rise to the formation of low velocity regions inside the exhaust system. This condition results in localized high-temperature regions in the exhaust volute casing, consequently impacting the insulation performance.

## Acknowledgment

The works were financed by Fundamental Research Funds for the Central Universities with a project number of 3122021045.

## Nomenclature

$HTC$ – convective heat transfer coefficient, [$Jm^{-2}s^{-1}°C^{-1}$]
$q$ – heat flux, [$Wm^{-2}$]
$q_m$ – mass-flow, [$kgs^{-1}$]
$T_{wall}$ – wall temperature, [°C]
$T_{out}$ – outflow temperature, [°C]
$P_{total}$ – total pressure, [Pa]
$P_{static}$ – static pressure, [Pa]
$T_{total}$ – total temperature, [°C]
$V_{axial}$ – axial fluid velocity, [$ms^{-1}$]
$V_{circ}$ – circumferential fluid velocity, [$ms^{-1}$]
$V_{radial}$ – radial fluid velocity, [$ms^{-1}$]

## References

[1] Wen, X.-Y., *et al.*, The History of Marine Gas Turbine Development in China, *Proceesing,* ASME Turbo Expo: Turbine Technical Conference and Exposition, San Antonio, Tex., USA, 2013, Vol. 5A, pp. 1-6
[2] Sun, T., *et al*., Performance Analysis of Marine Gas Turbine Elbow Type Exhaust Volute, *Journal of the Chinese Society Of Mechanical Engineers, 35* (2014), 5, pp. 405-412
[3] Gao, J., *et al*., Advances in Aerodynamics of Power Turbines for Marine and Aviation Applications, *Proceedings of the Institute of Mechanical Engineers, Part C: J. of Mechanical Engineering Science, 237* (2023), 22, pp. 5231-5246
[4] Yeranee, K., Rao, Y., A Review of Recent Studies on Rotating Internal Cooling for Gas Turbine Blades, *Chinese Journal of Aeronautics, 34* (2021), 7, pp. 85-113
[5] Gao, J., *et al*., Advances in Coupled Axial Turbine and Nonaxisymmetric Exhaust Volute Aerodynamics for Turbomachinery, *Proceedings of the Institution of Mechanical Engineers, Part G: Journal of Aerospace Engineering, 235* (2021), 9, pp. 981-993
[6] Lee, J., *et al*., Heat Exposure and Workers' Health: A Systematic Review, *Reviews on Environmental Health, 37* (2022), 1, pp. 45-59
[7] Park, J. S., *et al*., Effect of the Thermal Insulation on Generator and Micro Gas Turbine System, *Energy, 59* (2013), 8, pp. 581-589
[8] Singh, P., *et al.*, Studies on Stepped Air Ejector Diffusers incorporating Heat Transfer Effects, *International Journal of Turbo & Jet-Engines, 35* (2018), 3, pp. 251-263

[9] Park, C. H., *et al*., Experimental Verification of Thermal Insulation and Cooling for 500 W Class Micro Gas Turbine Generator, *Proceedings*, IEEE/ASME International Conference on Advanced Intelligent Mechatronics, Besacon, France, 2014, pp. 771-774
[10] Vinay, C. A., Chakravarthy, B., *Aerothermal Analysis of Insulation to Protect Exhaust Ducts of a Pusher Turbo Prop Engine Aircraft*, Lecture Notes in Mechanical Engineering, Springer-Heidelberg, Berlin, Germany, 2017, pp. 843-851
[11] Xu, R. S., *et al*. *Numerical Computation of Temperature in APU Compartment of Passenger Plane*, Applied Mechanics and Materials, Trans Tech Pubbications, Geneve, Switzerland, 2012, Vol. 220-223, pp. 855-858
[12] Pierre, A. C., Pajonk, G. M., Chemistry of Aerogels and Their Applications, *Chemical Reviews, 102* (2002), 11, pp. 4243-4266
[13] Randall, J. P., *et al*., Tailoring Mechanical Properties of Aerogels for Aerospace Applications, *ACS Applied Materials & Interfaces, 3* (2011), 3, pp. 613-626
[14] Smirnova, I., Gurikov, P., Aerogel Production: Current Status, Research Directions, and Future Opportunities, *The Journal of Supercritical Fluids*, *134* (2018), Apr., pp. 228-233
[15] Dai, J., *et al*., Study on the Thermal Insulation Property of $SiO_2$ Aerogel Influenced by the Phenolic Resin Pyrolysis Gas Permeation, *Heat Transfer Research, 52* (2021), 13, pp. 55-72
[16] Heyer, M., *et al*. Advanced Opacified Fiber-Reinforced Silica-Based Aerogel Composites for Superinsulation of Exhaust Tubing Systems in Semi-Stationary Motors, *Materials, 13* (2020), 12, 2677
[17] Fesmire, J. E., Sass, J. P., Aerogel Insulation Applications for Liquid Hydrogen Launch Vehicle Tanks, *Cryogenics, 48* (2008), 5-6, pp. 223-231
[18] Li, C. H,, *et al*. Research on Heat Transfer Characteristics of Nano-Porous Silica Aerogel Material and its Application on Mars Surface Mission, *Advanced Materials Research*, *924* (2014), Apr., pp. 329-335

Paper submitted: February 6, 2024
Paper revised: April 22, 2024
Paper accepted: May 9, 2024
2025 Published by the Vinča Institute of Nuclear Sciences, Belgrade, Serbia.
This is an open access article distributed under the CC BY-NC-ND 4.0 terms and conditions.